

# Lignin-based electrospun nanofiber membrane decorated with photo-Fenton Ag@MIF-100(Fe) heterojunctions for complex wastewater remediation

Guodong Tian<sup>1,2</sup>, Chao Duan (✉)<sup>1,2</sup>, Bingxu Zhou<sup>2</sup>, Chaochao Tian<sup>2</sup>, Qiang Wang (✉)<sup>1</sup>, Jiachuan Chen<sup>1</sup>

<sup>1</sup> State Key Laboratory of Biobased Material and Green Papermaking, Qilu University of Technology, Shandong Academy of Sciences, Jinan 250353, China

<sup>2</sup> College of Bioresources Chemical and Materials Engineering, Shaanxi University of Science and Technology, Xi'an 710021, China

© Higher Education Press 2023

**Abstract** Membrane technology for wastewater remediation has aroused wide interest owing to its unique properties and potential applications. However, it remains challenging to explore green, efficient and robust membrane material and technique for complex wastewater treatment. Herein, we proposed using a simple electrospinning and *in situ* seeding method to fabricate a lignin-based electrospun nanofiber membrane (LENM) decorated with photo-Fenton Ag@MIL-100(Fe) heterojunctions for efficient separation of oil/water emulsions and degradation of organic dye. Thanks to the embedded lignin in LENM, an ultrahigh MIL-100(Fe) loading (53 wt %) with good wettability and high porosity was obtained. As a result, the hybrid Ag@MIL-100(Fe)/LENM exhibited excellent oil/water emulsions separation efficiency (more than 97%) without a compromise of water flux. Moreover, the hybrid membrane showed an excellent dye removal with degradation of 99% methylene blue within 30 min under illumination, which is attributed to a synergy of dye adsorption/enrichment and photo-Fenton catalytic degradation from Ag@MIL-100(Fe). Therefore, the lignin-based photo-Fenton hybrid membrane can lay the foundation for the preparation and application of green, sustainable and versatile membrane materials and technologies for efficient complex wastewater remediation.

**Keywords** lignin, electrospinning, heterojunctions, photo-Fenton catalysis, wastewater remediation

## 1 Introduction

In light of the rapid industrialization and urbanization in recent decades, tens of thousands of hazardous contaminants, including organic dyes, oily wastewater, pesticide residues and so on, have been discharged into the surface water system without complete treatments, leading to a series of concerns on water pollution [1,2]. Normally, effluents from different industries, such as printing, textile, food, dyeing and finishing, consists of plenty of complex and toxic organic ingredients, which are hard to biodegrade and even harmful to human health [3]. Typically, organic dye has become one of the dominated pollutants due to its wide variety, large discharge and great harm, which has serious threats on the balance of ecological environment and even the safety of human beings [2,4]. To this end, many approaches have been adopted in an attempt to remediate the complex wastewater, such as adsorption [5], flocculation, electrocatalysis [6], chemical oxidation [7], membrane separation [8]. Among, membrane separation technology has energized tremendous research enthusiasm owing to its easy handling, small space occupancy, high efficiency and large-scale implementation [9,10]. However, conventional monofunctional and fossil-based membranes are prone to suffer membrane fouling, poor adaptability and performance deterioration, resulting in a reduced permeability and separation efficiency during the long-term run. Hence, it is extremely urgent to exploit a green, efficient and multifunctional membrane for the remediation of complex wastewater.

Electrospinning has been regarded as a versatile technique for preparation of multifunctional nanofiber composites [11]. In particular, electrospun nanofiber membrane (ENM) is favored because of its porous

Received December 3, 2022; accepted January 19, 2023;  
online May 10, 2023

E-mails: duanchaonba@126.com (Duan C.),  
wangqiang8303@163.com (Wang Q.)

structure, high specific surface area, and ease of modification [12]. To date, many petroleum-based polymers, such as polyacrylonitrile (PAN) [13], polyvinyl alcohol [14] and polyvinylidene fluoride [15], are the most common yet relatively high-cost and non-degradable precursors for electrospinning. In contrast, biomass materials such as lignin and cellulose, are of inherent nature, low cost, renewability and eco-friendliness, so they can be applied as excellent supplements or substitutes for conventional fossil-based precursors [16–18]. Lignin is a by-product from lignocellulose fractionation or pulp and paper industry. It is usually under a direct combustion for energy recovery rather than conversion into various value-added products, leading to an insufficient utilization of resource [19,20]. Therefore, lignin valorization is of great importance and under extensive research. For example, Yu et al. [21] had successfully fabricated lignin-based electrospun nanofibers (LENFs) using alkali lignin and PAN for reversible radioiodine capture and found that the adsorption capacity toward radioiodine raised with the increase of lignin content in LENFs. However, although the lignin embedding in ENMs can improve the performances of adsorption capacity, permeability and hydrophobicity, the non-degradation of contaminants and membrane fouling are still inevitable.

Inspiringly, it is an effective strategy to integrate some special catalysts into the LENMs so that some advanced oxidation processes like Fenton, photocatalytic degradation can be endowed [22]. On the other hand, the ENFs can enable the deposition and recovery of nano- or micro-catalysts, thus promoting their catalytic performance [23]. For the catalysts, metal–organic frameworks (MOFs) have emerged due to their high porosity, significant specific surface area, adaptable structure, and huge size, and easy chemical modification, which are beneficial to their catalytic activity [24–26]. Moreover, some MOFs, including Ti-, Zn-, Fe-, Co- and Zr-based MOF, demonstrate great advantage in photocatalysis because of their semiconductor-like features, e.g., broadened absorption of visible light, enhanced separation and transmission of photo-generated electron [24–26]. In addition, it is acknowledged that a variety of nanoparticles can be anchored to the surfaces of MOFs to create heterostructures, thus improving their photocatalytic efficiency [27–29]. For example, Xiao et al. [28] *in situ* synthesized the Pt NPs@ UiO-66-NH<sub>2</sub> photocatalytic heterojunctions to accelerate electron conduction and to prevent the recombination of photo-generated carriers, thus obtaining an enhanced photocatalytic activity. Liu et al. [29] deposited 2D TiO<sub>2</sub> nanosheets onto porous MIL-100(Fe) to prepare the sandwich-like TiO<sub>2</sub> NS@MIL-100(Fe) heterostructures. As a consequence, the adsorption capacity and photocatalytic degradation activity for methylene blue (MB) under visible light were significantly enhanced. In particular, apart from economic benefit, catalysts derived from Fe-based MOFs, like MIL-100 and MIL-53,

have an excellent adsorption capacity and deliver a photo-Fenton synergy, thus boosting the catalytic degradation of organic pollutants [30].

Herein, we propose using a lignin-based hybrid membrane, namely Ag@MIL-100(Fe)/LENM with a structure of core–sheath and photo-Fenton catalysis, for productive separation of emulsions and degradation of organic dyes in a complex wastewater. The lignin-based ENFs are served as core, while the well-deposited Ag nanoparticles on the surfaces of MIL-100(Fe) crystals, defined as Ag@MIL-100(Fe) heterojunctions, are functioned as photocatalytic sheath. It is hypothesized that (1) the introduction of lignin cannot only partially replace the PAN, but also provide more sites (function groups and rough surface) for the ultrahigh MIL-100 (Fe) loading; (2) the *in situ* immobilized Ag@MIL-100(Fe) with high porosity, hydrophilicity and photo-Fenton behaviors can endow the hybrid membrane with excellent membrane separation and adsorption-catalysis capacity. Both of them are responsible for the robust separation efficiency, membrane flux and photo-Fenton catalysis of the hybrid LENM toward a complex wastewater system.

---

## 2 Experimental

### 2.1 Materials

Lignin was extracted from a black liquor of bamboo kraft pulp. NaOH, *N,N*-dimethylformamide, ferrous chloride tetrahydrate (FeCl<sub>2</sub>·4H<sub>2</sub>O), H<sub>2</sub>O<sub>2</sub> (30 wt %), methylene blue (MB), AgNO<sub>3</sub>, cyclohexane, petroleum ether and rapeseed oil, were purchased from China Aladdin Reagent Co., Ltd. 1,3,5-Benzenetricarboxylic acid (H<sub>3</sub>BTC) and polyacrylonitrile (PAN, *M<sub>w</sub>* of 80000), ethylene diamine tetraacetic acid disodium salt (EDTA-2Na), benzoquinone (BQ) and *tert*-butyl alcohol (TBA) were purchased from Shanghai McLean Biochemical Co., Ltd. Deionized water was utilized throughout the experiment, and all the reagents were not subjected to further purification prior to use.

### 2.2 Preparation of LENM loaded with MIL-100(Fe) crystals

The preparation of different ratios of lignin/PAN ENM can refer to Electronic Supplementary Material (ESM), in which we selected the optimized electrospinning dope with lignin: PAN of 5:5 for follow-up experiments. According to the previous work of our research group [31], MIL-100(Fe)/LENM with core–sheath structure was fabricated by a simple *in situ* seeding synthesis. Specifically, 1.751 g of H<sub>3</sub>BTC was added to a beaker containing 1 mol·L<sup>-1</sup> NaOH solution, stirred to completely dissolve H<sub>3</sub>BTC, and it was used as solution A. Then, 2.26 g of FeCl<sub>2</sub>·4H<sub>2</sub>O were completely dissolved

in 100 mL of water to produce Solution B. Next, LENM pre-doped with a small amount of H<sub>3</sub>BTc was immersed in solution A for a period of time, and then solution B was dropwise added to solution A at room temperature, and stirred continuously for 24 h. To obtain MIL-100(Fe)/LENM, the lignin-based membrane loaded with MIL-100(Fe) was rinsed with deionized water prior to vacuum drying for at 50 °C for 5 h.

The loading amounts of MIL-100(Fe) or Ag nanoparticles on LENM can be calculated by the weight change of nanofiber membrane before and after loading, as demonstrated by the formula below:

$$\varphi = \frac{W_1 - W_0}{W_1} \times 100\%, \quad (1)$$

where  $W_1$  and  $W_0$  (g) refer to the mass of the electrospun membrane without and with the MIL-100(Fe) or Ag nanoparticles loading, respectively.  $\varphi$  is the loading rate of MIL-100(Fe) or Ag nanoparticles on electrospun membrane.

### 2.3 Preparation of Ag@MIL-100(Fe)/LENM

The immobilization of Ag nanoparticles onto the surfaces of MIL-100(Fe)/LENM was achieved using a method described in the literature [32,33]. In short, MIL-100(Fe)/LENM was submerged in 30 mL AgNO<sub>3</sub> solution with 1 g·mL<sup>-1</sup> concentration and then transferred it to a photocatalytic reactor. The aforementioned solution was exposed to ultraviolet light under magnetic stirring for 60 min. By virtue of the photo-reduction and some reducing groups in lignin, a great number of Ag nanoparticles were successfully anchored on the surface of MIL-100(Fe)/LENM.

### 2.4 Oil/water emulsions preparation and separation

According to previously reported literature [34], the surfactant-stabilized emulsions (SSEs) and surfactant-free emulsions (SFEs) were prepared by using cyclohexane, petroleum ether and rapeseed oil. Specifically, SFEs were obtained by mixing 2 mL of oil and 98 mL of water and by ultrasonic mixing at room temperature for 30 min. For SSEs, a set of stable oil/water emulsions were obtained by adding 15 mg Tween 80 in advance as emulsifier into the same oil–water mixture and then mixing for 30 min.

The membrane flux ( $J$ ) of the composite membrane at 0.01 MPa (L·m<sup>-2</sup>·h<sup>-1</sup>) can be calculated as per the formula:

$$J = \frac{V}{S \times t}. \quad (2)$$

In the formula,  $V$  (L),  $t$  (h) and  $S$  (m<sup>2</sup>) correspond to the permeable water volume, filtration time and area, respectively. A ultraviolet–visible (UV–vis) spectrophotometer was used to determine the oil contents before and after separation. The separation efficiency ( $R$ , %) can be

obtained using the formula as follows:

$$R = \left(1 - \frac{C_f}{C_0}\right) \times 100\%, \quad (3)$$

where  $C_0$  and  $C_f$  refer to the oil content in the oil/water emulsions before and after separation, respectively.

### 2.5 Evaluation of adsorption-photo-Fenton catalytic performance of the hybrid membrane

Organic dye MB was chosen as the model pollutant to examine the adsorption capacity and photo-Fenton catalysis of the membrane. Typically, 15 mg sample and 60 mL solution of MB at an starting concentration of 50 mg·L<sup>-1</sup> were placed in a 250 mL glass bottle, initial pH 7 was adjusted and stirred in a 25 °C water bath at 150 r·min<sup>-1</sup>. To measure the MB concentration in the aqueous solution, 2 mL of the reacted solution were piped out periodically for UV–vis detection during the adsorption process. The sample's adsorption capacity is determined as per the formula:

$$q_t = \frac{(C_0 - C_t) \times V}{m}, \quad (4)$$

where  $q_t$  (mg·g<sup>-1</sup>) is the mass of dye adsorbed by LENM at random time,  $m$  is the mass of dried LENM (g),  $V$  is the volume of the MB solution.  $C_0$  and  $C_t$  refer to dye concentrations prior to and following membrane adsorption, respectively.

The adsorption process was analyzed by quasi-first-order kinetic model, and the linear equation was represented as:

$$\log(q_e - q_t) = \log q_e - k_1 t, \quad (5)$$

where  $q_e$  and  $q_t$  (mg·g<sup>-1</sup>) present the equilibrium adsorption and regular adsorption capacity at random time ( $t$ , min), respectively.  $k_1$  (min<sup>-1</sup>) refers to adsorption rate constant in quasi-first-order model.

The adsorption-photo-Fenton performance of the hybrid membrane was under comprehensive assessment through catalytic degradation experiment of MB. It was conducted in a photo-catalytic reactor equipped with multi tubes. To simulate sunshine, a 500 W xenon lamp with a 420 nm filter was used. In brief, to achieve equilibrium adsorption, 10 mg of the sample was placed into a glass bottle containing 30 mL of MB solution with a pristine concentration of 20 mg·L<sup>-1</sup>. The original pH value was then adjusted to 7 and agitated in the dark at 150 r·min<sup>-1</sup> for 1 h. Then the xenon lamp was turned on and 50 μL H<sub>2</sub>O<sub>2</sub> solution was immediately added to initiate the catalysis. The concentration of remaining MB in the solution was measured using the UV–vis absorbance at 664 nm of 2 mL solution that was collected from the bulk solution at regular intervals during the catalytic degradation process. A quantity of quenching agents (EDTA-2Na, BQ and TBA) were respectively added into the reaction solution prior to the addition of

$\text{H}_2\text{O}_2$  to study the role of holes ( $\text{h}^+$ ), superoxide radicals ( $\cdot\text{O}_2^-$ ) and hydroxyl radicals ( $\cdot\text{OH}$ ) on the degradation of MB.

### 3 Results and discussion

#### 3.1 Synthesis and morphology of lignin-based photo-Fenton catalytic membrane

Figure 1 illustrates the synthesis and morphologic

characterization of the hybrid LENM decorated with photo-Fenton  $\text{Ag}@MIL-100(\text{Fe})$  catalyst via electrospinning and *in situ* seeding strategy. As shown in Fig. 1(a), three key steps are involved in the preparation of the hybrid membrane. Initially, different proportions of PAN and lignin, including 10:0, 8:2, 5:5, 4:6 (on weight basis) and a few of pre-doped ligand  $\text{H}_3\text{BTC}$  (seeding method) were selected as spinning dope to obtain various lignin-based nanofiber membranes. Then, the lignin and  $\text{H}_3\text{BTC}$  with abundant of phenolic hydroxyl and carboxylic acid groups serve as reaction sites to coordinate the  $\text{Fe}^{2+}$ .

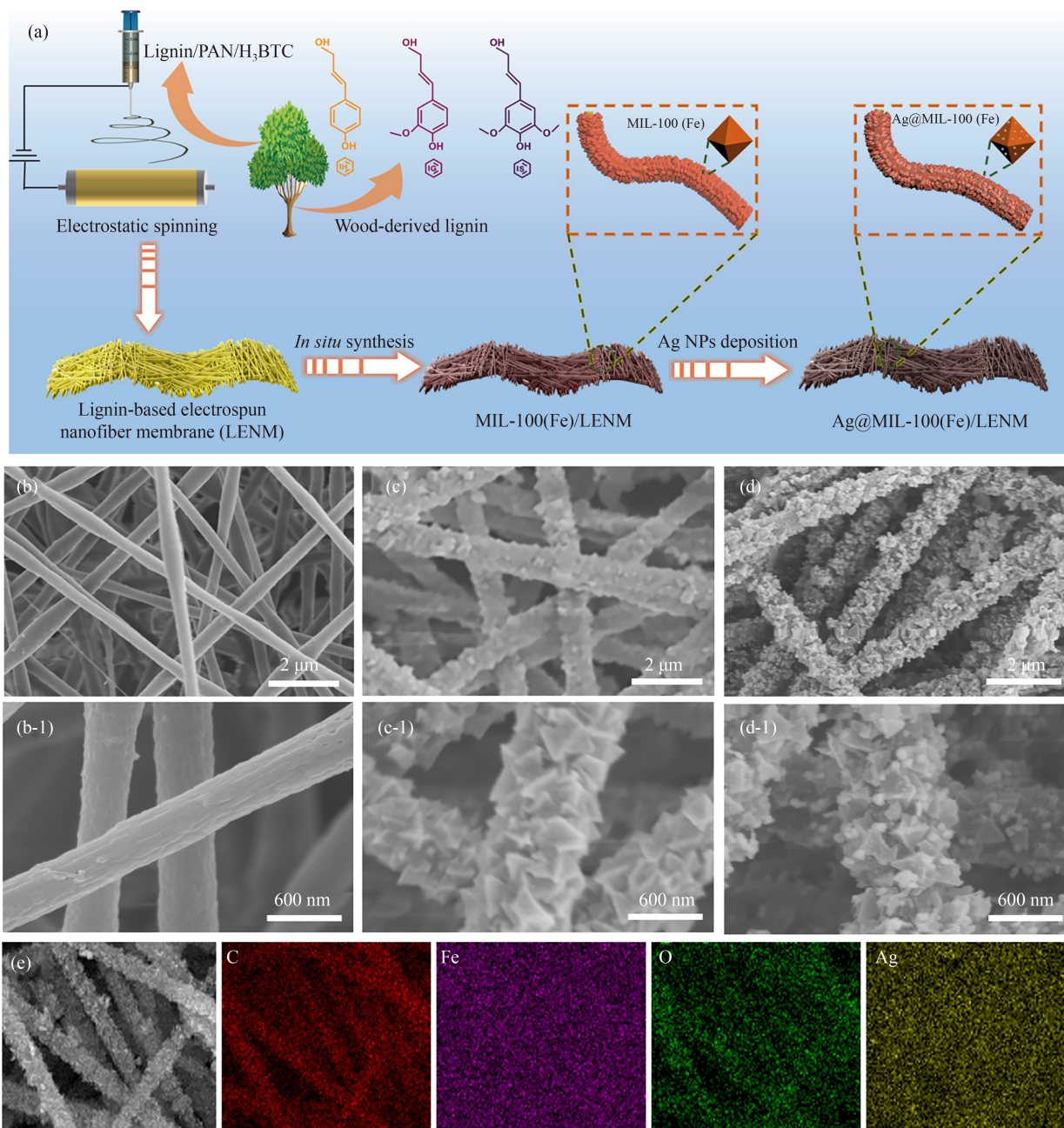


**Fig. 1** (a) Schematic diagram of the synthesis of photo-Fenton lignin-based  $\text{Ag}@MIL-100(\text{Fe})/\text{LENM}$ ; (b–d) SEM images of LENM,  $MIL-100(\text{Fe})/\text{LENM}$  and  $\text{Ag}@MIL-100(\text{Fe})/\text{LENM}$  at the optimized 50 wt % of lignin content; (e) EDS mapping images of  $\text{Ag}@MIL-100(\text{Fe})/\text{LENM}$  with C, Fe, O, Ag element.

Therefore, vast majority of MIL-100(Fe) crystals are firmly and uniformly wrapped around the nanofibers. Finally, a mass of photo-reduced Ag nanoparticles are uniformly deposited and dispersed on the surfaces of MOFs to form the heterojunctions, further enhancing the hybrid membrane's photo-Fenton catalytic performance [35]. Table S1 (cf. ESM) shows the weight and weight fraction of LENM, MIL-100(Fe) and Ag nanoparticles in final hybrid membrane.

The effects of different lignin contents on the morphology of LENMs were investigated (Fig. S1, cf. ESM). Evidently, as the lignin content increases (0, 20, 50 and 60 wt %), the color of membrane gradually deepens from light white to brown black. Besides, the ENFs with increased diameter and roughened surface, such as some grooves and pores, can be observed (Figs. S1(a–d)). Nevertheless, once the lignin content raises to 60 wt %, some aggregations and tumefactions of nanofibers occur (Figs. S1(d-1, d-2)), impairing the properties and performance of LENMs. Therefore, 50 wt % of lignin content (lignin: PAN = 5:5) in the mixture dope was chosen as the optimum one for the next experiment and analyses. The lignin embedding would facilitate the next MOFs immobilization and dye adsorption [21]. For instance, the variation of MOFs loading was shown in Fig. S2 (cf. ESM). The MOFs loading increases from 20 (lignin free) to 53 wt % (Fig. S2(a)), and the equilibrium adsorption of organic dye raises from 7.5 to 28.5 mg·g<sup>-1</sup> (Fig. S2(b)) when the lignin content is up to 53 wt %.

Figures 1(b–d) show the changes of morphology of the hybrid LENMs in each stage. For the pristine nanofibers (Figs. 1(b), 1(b-1)), the average diameter is about 450 nm and rough surfaces can be observed due to the addition of lignin, which is consistent with literature that reported by Ahmad et al. [36]. Upon the *in situ* synthesis via seeding method, plenty of octahedral MIL-100(Fe) crystals are uniformly immobilized and wrapped around the LENFs, forming a unique “core–sheath” structure (Figs. 1(c), 1(c-1)). As a result of photo-reduction of silver nitrate precursor, a quantity of Ag nanoparticles was well anchored and dispersed on the surfaces of MOFs (Figs. 1(d), 1(d-1)), which are responsible for the enhanced photo-Fenton catalytic performance of the hybrid membrane. Moreover, the element mapping images of Ag@MIL-100(Fe)/LENM clearly show the existence of C, O, Ag and Fe elements (Fig. 1(e)), which further proves the successful preparation of the lignin-based hybrid membrane.

### 3.2 Structural features of lignin-based photo-Fenton catalytic LENM

The pore structures of LENM, MIL-100(Fe)/LENM, Ag@MIL-100(Fe)/LENM and pure MIL-100(Fe) with respect to specific surface area (SSA), mean pore diameter (MPD) and pore size distribution were

investigated (Fig. 2). As shown in Fig. 2(a), MIL-100(Fe) shows a typical isotherm between type I and IV, and MIL-100(Fe)/LENM shows typical type I isotherms based on the N<sub>2</sub> adsorption and desorption isotherms, revealing the presence of micropores and mesopores. These results are in agreement with the pore size distribution that was illustrated in Fig. 2(b). Moreover, the SSA of LENM is only 5.8 m<sup>2</sup>·g<sup>-1</sup>, and it significantly increases to 793.6 m<sup>2</sup>·g<sup>-1</sup> (MIL-100(Fe)/LENM) when immobilizes the porous MIL-100(Fe) crystals with ultrahigh SSA of 1214.4 m<sup>2</sup>·g<sup>-1</sup> (Fig. 2(c)). Based on the results of pore size distribution, vast majority of pores in the MIL-100(Fe) and MIL-100(Fe)/LENM samples belong to micropores, ranging from 1.2–3.0 nm, and their MPD are 2.6 and 2.2 nm, respectively (Fig. 2(d)). Additionally, compared with MIL-100(Fe)/LENM, the SSA, and MPD of Ag@MIL-100(Fe)/LENM had negligible changes, only slight decreases to 772.8 m<sup>2</sup>·g<sup>-1</sup> and 2.5 nm, indicating that the deposition of Ag nanoparticles onto the surfaces of MOFs had negligible effect on the pore structure and pore size distribution of the photo-Fenton catalyst. These results indicate that the MOFs immobilization can indeed improve the SSA and porosity of hybrid membranes, which would be beneficial to the adsorption of organic pollutants.

Some other structural properties, including crystal structure, chemical structure and composition are illustrated in Fig. 3. For the crystal structure in XRD spectra (Fig. 3(a)), two peaks at 9.2° and 16.8° in the LENM sample are attributed to lignin and PAN, respectively [37,38]. Besides, some peaks at 10.3°, 11.0°, 12.5° and 20.2° assigned to MIL-100(Fe) [39], are also presented in those samples of MIL-100(Fe)/LENM and Ag@MIL-100(Fe)/LENM, confirming the successful synthesis of MIL-100(Fe) on nanofibers. Similarly, the characteristic peak at 38.1° and the weak diffraction peak at 42.0° are attributed to Ag nanoparticles [40], which indicates that the successful deposition of Ag nanoparticles on MIL-100(Fe) surface. For the chemical structure in Fig. 3(b), the LENM displays the combination of characteristic peaks of lignin and PAN. More precisely, peak at 3510 cm<sup>-1</sup> is assigned to –OH; peaks at 1600, 1510 and 1425 cm<sup>-1</sup> are caused by aromatic ring of lignin; the other peaks at 1263, 1128 and 1022 cm<sup>-1</sup>, attributed to C–O, C–C and aromatic C–H vibrations of guaiacyl ring of lignin, respectively [41]. Besides, the peak at 2240 cm<sup>-1</sup> is caused by C–N stretching from PAN [42]. For MIL-100(Fe)/LENM and Ag@MIL-100(Fe)/LENM, the characteristic peaks at 710 and 760 cm<sup>-1</sup> belongs to Fe–O vibration, while the peaks at 1378 and 1448 cm<sup>-1</sup> can be assigned to C=C vibration from benzene ring [43]. The MIL-100(Fe) sample's spectrum shows the peaks mentioned above, proving the MIL-100(Fe) particles were effectively deposited on LENFs.

XPS patterns of Ag@MIL-100(Fe)/LENM are shown in Figs. 3(c–f). The C, O, Fe and Ag element is presented

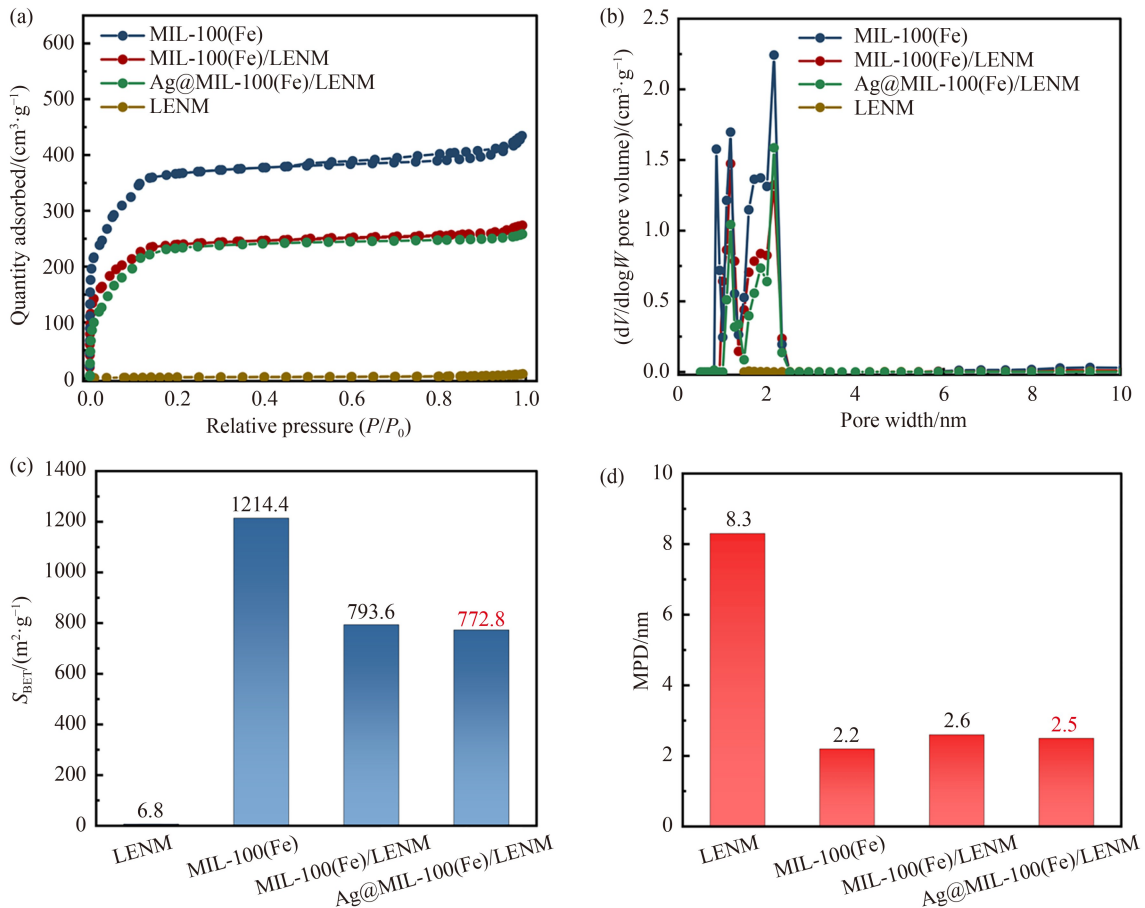


**Fig. 2** BET results based on the (a) N<sub>2</sub> adsorption/desorption isotherms, (b) pore size distribution (PSD), (c) specific surface area (SSA), (d) mean pore diameter (MPD) of LENM, MIL-100(Fe), MIL-100(Fe)/LENM and Ag@MIL-100(Fe)/LENM.

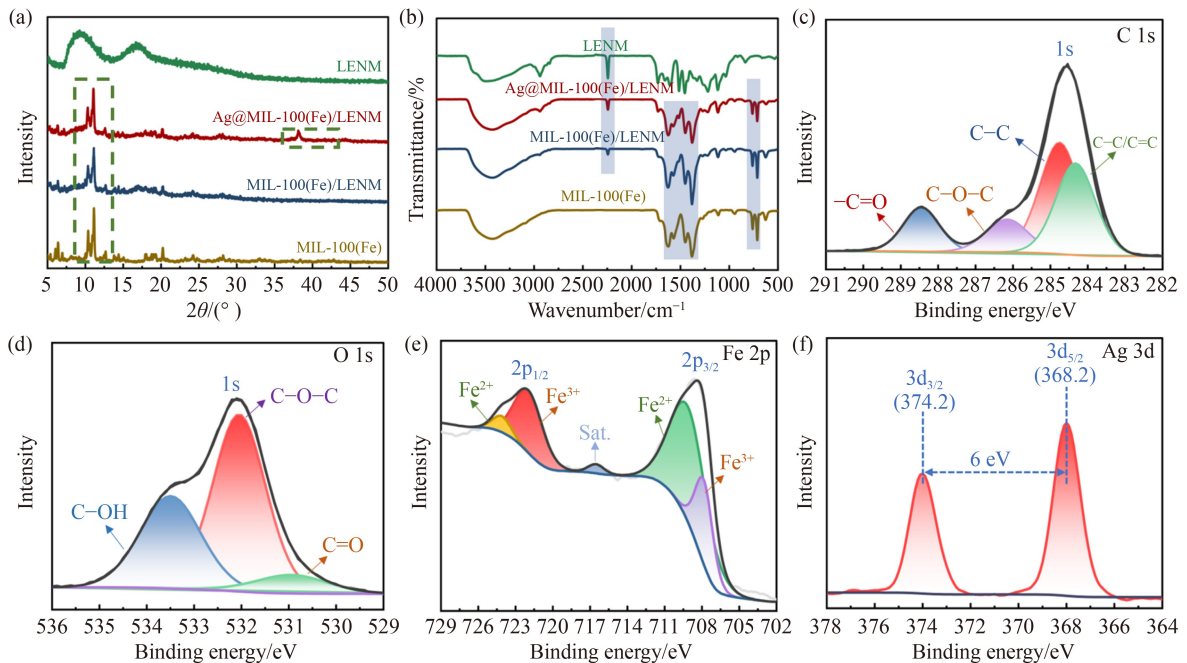


**Fig. 3** (a) XRD patterns and (b) Fourier transform infrared spectra of MIL-100(Fe) particles, MIL-100(Fe)/LENM, Ag@MIL-100(Fe)/LENM and LENM; XPS spectra of Ag@MIL-100(Fe)/LENM (c) C 1s, (d) O 1s, (e) Fe 2p and (f) Ag 3d.

in each spectrum. In Fig. 3(c), the signals of C 1s at 284.8 and 288.9 eV derived from the H<sub>3</sub>BTC of MIL-100(Fe), while the signals at 284.8 and 287.1 eV are assigned to C–O–C and C–OH in lignin, respectively [43,44]. In the O 1s spectra (Fig. 3(d)), three peaks at 530.8, 532.1 and 534.1 eV respectively attributed to C=O, C–O–C and C–OH in lignin and MOFs [43,44], indicating that there is a mass of oxygen-containing functional groups in the hybrid membrane. In Fig. 3(e), two peaks at 724.3 and 709.8 eV caused by 2p<sub>1/2</sub> and 2p<sub>3/2</sub> of Fe, respectively, while the satellite peak at 718 eV is attributed to Fe (III) in MIL-100(Fe) [43]. As shown in Fig. 3(f), the signal of Ag 3d displays two main peaks at 374.2 and 368.2 eV, corresponding to 3d<sub>3/2</sub> and 3d<sub>5/2</sub> of Ag, respectively [45,46]. The two peaks were spaced 6.0 eV, both of which were characteristic peaks of zero-valent Ag, implied a fact that Ag species were elemental Ag. Similar results were also reported in the literature. For examples, Zhang et al. [35] synthesized Ag/MXene photocatalysts and confirmed that the Ag species were elemental silver using XPS method. Therefore, the XPS results above further confirm that the synthesis and immobilization of Ag@MIL-100(Fe) on LENM has completed.

### 3.3 Wettability and separation ability of oil/water emulsions from Ag@MIL-100(Fe)/LENM

Figure 4 shows the wettability and oil–water separation ability of the membrane. As shown in Fig. 4(a), the water contact angle (WCA), indicator of wettability of the membrane, was investigated. Since the inherent hydrophobicity of kraft lignin, the initial LENM had a high WCA (123.7° at 1 s), which means a relative low wettability. In contrast, after the MOF loading, both the MIL-

100(Fe)/LENM and Ag@MIL-100(Fe)/LENM membranes show a significant increase of wettability, almost 0° of WCA at 0.1 s. The enhanced wettability is mainly due to the rougher surface and more hydrophilic groups (–COOH) in MIL-100(Fe) [47]. Thanks to the high hydrophilicity, rough surface and interfacial capillary effect, a large amount of water can be absorbed and reserved in the nanofiber network. As a result, a unique hydration layer can be developed on the surface of the modified membrane to effectively resist the permeability of oil droplets (Fig. S3, cf. ESM) [48]. As shown in Fig. 4(b), the pristine oily emulsions are of high turbidity with evident oil droplets based on the microscope image. On the contrary, an oil-free filtrate with high transparency can be obtained as a result of the membrane filtration.

The separation capacities toward different oil-based emulsions (cyclohexane, petroleum ether, rapeseed oil) were investigated in terms of permeation flux and separation efficiency. As shown in Fig. 4(c), the permeation fluxes toward cyclohexane-, petroleum ether- and rapeseed oil-based SFEs are of 6990.5, 6866.3 and 7809.9 L·m<sup>2</sup>·h<sup>−1</sup>, respectively. Although the membrane fluxes for SSEs are not as good as the formers, they remain at a high level, showing 2537.6, 2366.0 and 3216.8 L·m<sup>2</sup>·h<sup>−1</sup> for each emulsion, respectively. Correspondingly, the separation efficiency of the hybrid membrane in all cases is higher than 97% (Fig. 4(d)) and only decreases slightly (about 2%) after five filtration cycles (Fig. S4, cf. ESM). In addition, no trace of oil can be found in the filtrates based on the UV–vis spectra result (Fig. S5, cf. ESM). These results above justify that the Ag@MIL-100(Fe)/LENM has remarkable oil/water emulsions separation performance and demonstrates excellent promise for a sophisticated oily wastewater cleanup.

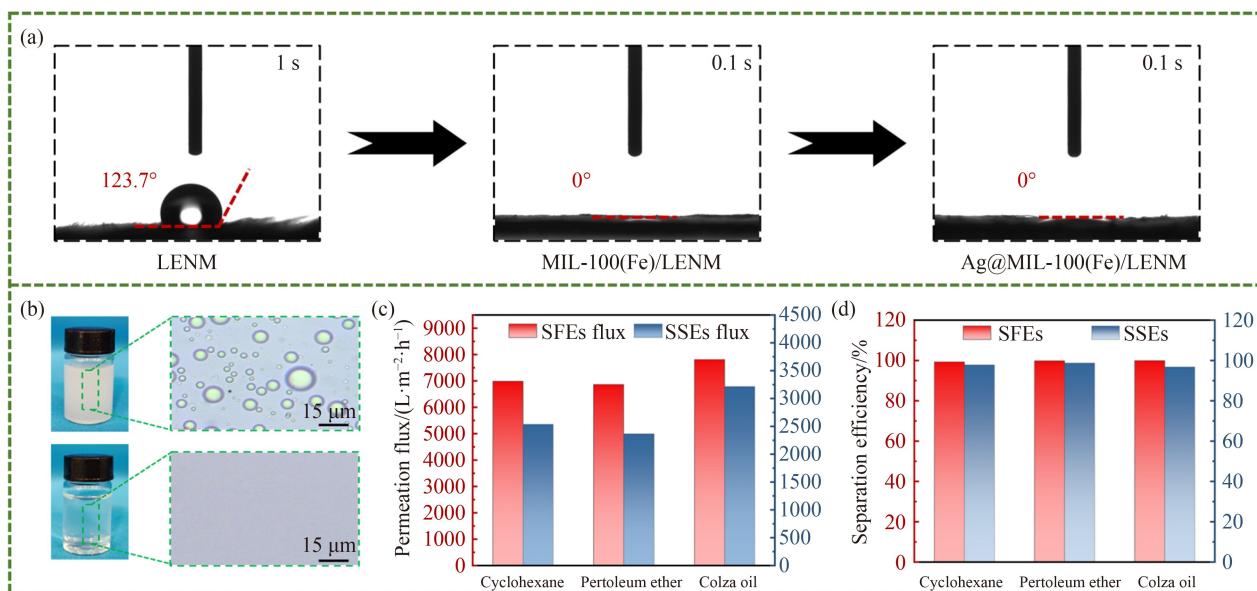


**Fig. 4** (a) WCA results of different samples; (b) photographs and optical microscope pictures of oil/water emulsion pre- and post-separation; (c) permeation fluxes and (d) separation efficiency of SFEs and SSEs filtrated by the Ag@MIL-100(Fe)/LENM.

### 3.4 Dye adsorption and photo-Fenton catalysis of Ag@MIL-100(Fe)/LENM

Figure 5 shows the adsorption and photo-Fenton catalytic degradation performance of the membrane for dyes. The synergy of adsorption and catalysis of Ag@MIL-100(Fe)/LENM under light were evaluated using MB as simulated organic dye wastewater. As shown in Fig. 5(a), there is a relatively low absorption band for LENM because of the presence of lignin. Instead, benefiting from a good light absorption ability of Fe-based MOF, the absorption band of MIL-100(Fe)/LENM at the visible light (420–600 nm), obviously increases and further promotes in the case of Ag@MIL-100(Fe). This is attributed to the plasma effect on the Ag nanoparticles surface, which significantly enhances its light absorption capacity [35]. These results indicate that Ag@MIL-100(Fe)/LENM is capable to absorb more visible light/energy, thus promoting more generation of photo-induced electron and radical groups ( $\cdot\text{OH}$  or  $\cdot\text{O}_2^-$ ) to degrade the organic pollutants. Similarly, the results of photoluminescence (PL) spectra in Fig. 5(b) are in agreement with their light adsorption (Fig. 5(a)). Admittedly, the lower PL intensity at 565 nm, the higher separation efficiency of photo-generated carrier. This is due to the strong conductivity of Ag nanoparticles further facilitated the efficient separation of photo-generated charges [35,46]. Based on that, the Ag@MIL-100(Fe)/LENM possesses the most robust photocatalytic ability due to its enhanced photo-induced electron–hole separation efficiency and light absorption

ability. In addition, as shown in Fig. 5(c), the results of adsorption kinetics reveal that the LENM has a certain yet relatively low equilibrium adsorption (about  $27.5 \text{ mg}\cdot\text{g}^{-1}$ ) toward MB dye due to the presence of lignin in the nanofiber network (Fig. S2). In contrast, thanks to the immobilization of porous MIL-100(Fe), the adsorption capacity of Ag@MIL-100(Fe)/LENM is significantly improved, showing the highest adsorption capacity ( $\sim 140 \text{ mg}\cdot\text{g}^{-1}$ ) and rate. Figure 5(d) illustrates the changes of MB absorbance as function of the hybrid membrane treatment for different treatment time. Evidently, MB solution initially shows a notable absorbance at 664 nm and finally vanished as a result of photo-Fenton treatment for 30 min (also supported by the color changes in inserts). As shown in Fig. 5(e), under the dark condition, the LENM, MIL-100(Fe)/LENM and Ag@MIL-100(Fe)/LENM adsorbed approximately 30%, 50% and 58% of MB dye, respectively. Upon the visible light irradiation, the concentration of MB slightly decreases in the case of LENM, while under the action of photocatalysts of MIL-100(Fe) and Ag@MIL-100(Fe), the concentration of MB decreased significantly. Inspiringly, due to the photo-Fenton synergy from the Ag@MIL-100(Fe) heterojunction, the hybrid membrane achieved a complete degradation of MB dye with 30 min of illumination. Moreover, the corresponding kinetic constant ( $k$ ) of photocatalytic degradation of MB was fitted (Fig. 5(f)) and the  $k$  values of LENM (0.0034), MIL-100(Fe)/LENM (0.0786) and Ag@MIL-100(Fe)/LENM (0.1415) are in an ascending order, which indicates that the resultant

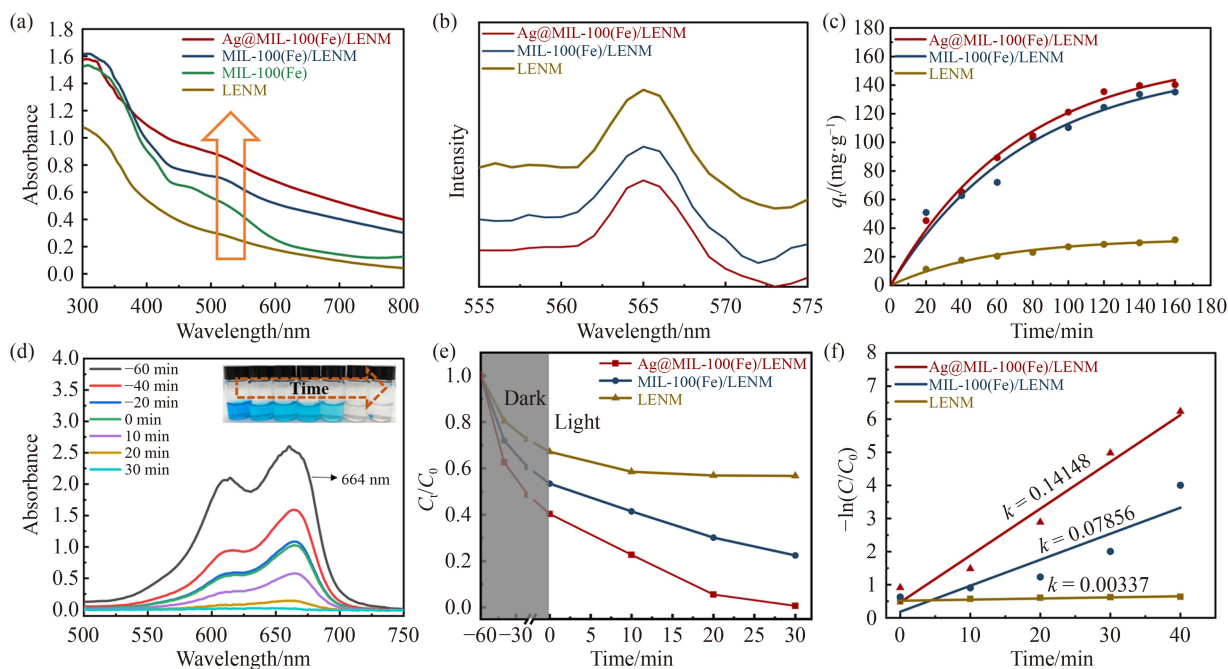


**Fig. 5** (a) UV-vis DRS and (b) PL spectrum of LENM, MIL-100(Fe), MIL-100(Fe)/LENM and Ag@MIL-100(Fe)/LENM; (c) comparison of adsorption capacity of three different lignin-based membranes; (d) UV-vis adsorption spectra of MB during the treatment of Ag@MIL-100(Fe)/LENM; (e) adsorption capacity and photo-Fenton catalytic activity of the three different membranes under dark and visible light conditions; (f) kinetic curves for the three membrane samples.

hybrid membrane has the strongest catalytic activity. Furthermore, to investigate the specific active substance in this catalytic system, some free radical scavengers, such as EDTA-2Na, BQ and TBA are used for selectively trapping  $h^+$ ,  $\cdot O_2^-$  and  $\cdot OH$ , respectively [49]. As shown in Fig. S6 (cf. ESM), the catalytic degradation efficiency Ag@MIL-100(Fe)/LENM was 99.7% and it gradually decreased upon the addition of different free radical scavengers. Evidently, the addition of TBA exerted the most remarkable impact on the degradation efficiency (27.4%), followed by BQ (68.1%) and EDTA-2Na (80.7%), confirming that  $\cdot OH$  and  $\cdot O_2^-$  were dominant active species that contributed to the photocatalytic degradation of organic pollutant. The above results further confirm that the high conductivity of Ag nanoparticles and plasma effect significantly enhance the effective separation of photoinduced electron/hole from MOFs, thus facilitating the photocatalytic activity of the hybrid membrane to obtain a higher catalytic degradation efficiency [46]. Furthermore, we compared the degradation performance of Ag@MIL-100(Fe)/LENM with some other photocatalysts reported in the literature (Table S2, cf. ESM). Owing to the adsorption-photo-Fenton synergy, the Ag@MIL-100(Fe)/LENM in our work demonstrates an excellent performance and efficiency of dye removal among those photocatalytic materials.

### 3.5 Possible mechanism of adsorption-photo-Fenton synergy

The mechanism of adsorption-photo-Fenton synergy of Ag@MIL-100(Fe)/LENM for catalytic degradation dye was demonstrated in Fig. 6. As for the adsorption mechanism, the interactions between the hybrid membrane and MB dye may consist of pore capture, hydrogen bonding and  $\pi$ - $\pi$  stacking [13,50]. Initially, Ag@MIL-100(Fe)/LENM can adsorb and enrich MB dye because of

its abundant porous structure and large specific surface area (supporting data in Fig. 2). Specifically, MIL-100(Fe) on the fiber membranes possesses excellent porosity and high binding ability. Additionally,  $\pi$ - $\pi$  stacking between the benzene rings of dyes and the benzene rings in MIL-100(Fe) also contributes to the adsorption of dyes [51]. Due to their good adsorption capacity toward organic pollutants, MB can be captured by MIL-100(Fe) during the filtration process. Upon being exposed to visible light, the reserved MB underwent photo-Fenton degradation. In fact, during the photocatalytic process, the valence band electrons ( $e^-$ ) on the surface of Ag@MIL-100(Fe) are excited to the conduction band when the irradiated visible light exceeds its band gap energy, left the  $h^+$  in the valence band. The Ag nanoparticles deposited on MIL-100(Fe) surfaces further promote the effective separation of photoinduced electron/hole due to their high conductivity. Consequently, the separated  $e^-$  and  $h^+$  are capable of reacting with  $O_2$  and  $H_2O$  to generate a set of strong oxidative radicals, such as  $\cdot O_2^-$  and  $\cdot OH$ , both of which are responsible for the fast oxidative degradation of organic pollutants. In addition, a synergy of photo-Fenton catalysis derived from the integration of iron ions ( $Fe^{2+}$ ),  $H_2O_2$  and visible light can further boost the degradation process above [52].

## 4 Conclusions

In conclusion, the photo-Fenton catalyst of Ag@MIL-100(Fe) heterojunctions were successfully *in situ* immobilized on the LENM. Thanks to the introduction of lignin, the nanofiber in LENM matrix exhibits rough surfaces and high porosity, which are responsible for the relative high immobilization of MIL-100(Fe) crystals (53%). Owing to the inherent porosity and hydrophilicity

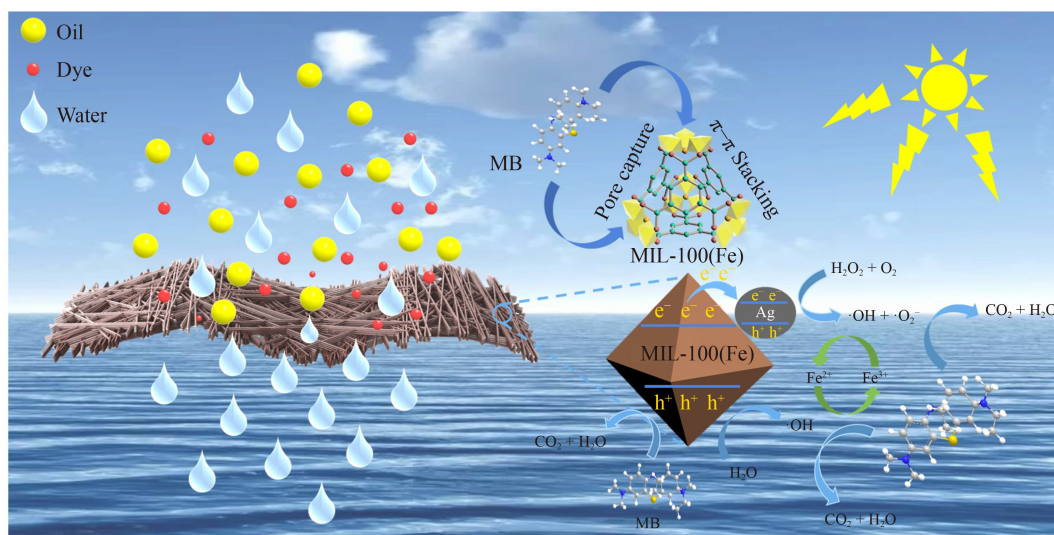


**Fig. 6** The possible adsorption-photo-Fenton mechanism of Ag@MIL-100(Fe)/LENM for catalytic degradation of MB dyes.

of MOF, the hybrid membrane shows a good wettability with  $0^\circ$  of WCA, thus endowing an efficient separation ( $>97\%$ ) and permeation flux ( $>2500 \text{ L}\cdot\text{m}^{-2}\cdot\text{h}^{-1}$ ) for oil/water emulsions. Moreover, the well-deposited Ag nanoparticles on surfaces of MOFs gave rise to an enhanced photo-Fenton effect. Therefore, the photo-Fenton catalysis, together with the dye adsorption/enrichment, tremendously endowed the Ag@MIL-100(Fe)/LENM excellent catalytic degradation toward MB dye. For examples, with 30 min of illumination, the hybrid membrane achieved a removal rate of more than 99% for MB. Based on the results above, the photo-Fenton hybrid LENM has a good prospect for the remediation of complex wastewater treatment, and this work may provide reference for fabricating green, sustainable and versatile membrane materials and technologies for wastewater treatment.

**Conflicts of interest** There are no conflicts to declare.

**Acknowledgements** The authors would like to acknowledge the financial support of the National Natural Science Foundation of China (Grant No. 22178206) and the Foundation of State Key Laboratory of Biobased Material and Green Papermaking (Grant No. GZKF202025), Qilu University of Technology, Shandong Academy of Sciences.

**Electronic Supplementary Material** Supplementary material is available in the online version of this article at <https://doi.org/10.1007/s11705-023-2309-9> and is accessible for authorized users.

## References

1. Yu L, Han M, He F. A review of treating oily wastewater. *Arabian Journal of Chemistry*, 2017, 10: S1913–S1922
2. Uddin F. Environmental hazard in textile dyeing wastewater from local textile industry. *Cellulose*, 2021, 28(17): 10715–10739
3. Methneni N, Morales Gonzalez J A, Jaziri A, Ben Mansour H, Fernandez Serrano M. Persistent organic and inorganic pollutants in the effluents from the textile dyeing industries: ecotoxicology appraisal via a battery of biotests. *Environmental Research*, 2021, 196: 110956
4. Saeed M, Muneer M, Akram N. Photocatalysis: an effective tool for photodegradation of dyes—A review. *Environmental Science and Pollution Research International*, 2022, 29(1): 293–311
5. Selvasembian R, Gwenzi W, Chaukura N, Mthembu S. Recent advances in the polyurethane-based adsorbents for the decontamination of hazardous wastewater pollutants. *Journal of Hazardous Materials*, 2021, 417: 125960
6. Shen M, Hu W, Duan C, Li J, Ding S, Zhang L, Zhu J, Ni Y. Cellulose nanofibers carbon aerogel based single-cobalt-atom catalyst for high-efficiency oxygen reduction and zinc–air battery. *Journal of Colloid and Interface Science*, 2023, 629: 778–785
7. Yan H, Lai C, Wang D, Liu S, Li X, Zhou X, Yi H, Li B, Zhang M, Li L, Liu X, Qin L, Fu Y. *In situ* chemical oxidation: peroxide or persulfate coupled with membrane technology for wastewater treatment. *Journal of Materials Chemistry A*, 2021, 9(20): 11944–11960
8. Jiang Y, Li S, Su J, Lv X, Liu S, Su B. Two dimensional COFs as ultra-thin interlayer to build TFN hollow fiber nanofiltration membrane for desalination and heavy metal wastewater treatment. *Journal of Membrane Science*, 2021, 635: 119523
9. Yang J, Li Z, Wang Z, Yuan S, Li Y, Zhao W, Zhang X. 2D material based thin-film nanocomposite membranes for water treatment. *Advanced Materials Technologies*, 2021, 6(10): 2000862
10. Long X, Zhao G, Hu J, Zheng Y, Zhang J, Zuo Y, Jiao F. Cracked-earth-like titanium carbide MXene membranes with abundant hydroxyl groups for oil-in-water emulsion separation. *Journal of Colloid and Interface Science*, 2022, 607: 378–388
11. Liao Y, Loh C H, Tian M, Wang R, Fane A G. Progress in electrospun polymeric nanofibrous membranes for water treatment: fabrication, modification and applications. *Progress in Polymer Science*, 2018, 77: 69–94
12. Zhu F, Zheng Y, Zhang B, Dai Y. A critical review on the electrospun nanofibrous membranes for the adsorption of heavy metals in water treatment. *Journal of Hazardous Materials*, 2021, 401: 12368
13. Zhao R, Tian Y, Li S, Ma T, Lei H, Zhu G. An electrospun fiber based metal–organic framework composite membrane for fast, continuous, and simultaneous removal of insoluble and soluble contaminants from water. *Journal of Materials Chemistry A*, 2019, 7(39): 22559–22570
14. Kang S K, Hwang K, Park J W, Ha Kim M, Lee P S, Jeong S H. Nanostructural engineering of electrospun poly(vinyl alcohol)/carbon nanotube mats into dense films for alcohol dehydration. *ACS Sustainable Chemistry & Engineering*, 2022, 10(40): 13380–13389
15. Lee E J, An A K, Hadi P, Lee S, Woo Y C, Shon H K. Advanced multi-nozzle electrospun functionalized titanium dioxide/polyvinylidene fluoride-co-hexafluoropropylene (TiO<sub>2</sub>/PVDF-HFP) composite membranes for direct contact membrane distillation. *Journal of Membrane Science*, 2017, 524: 712–720
16. Borrego M, Martín Alfonso J E, Sanchez M C, Valencia C, Franco J M. Electrospun lignin-PVP nanofibers and their ability for structuring oil. *International Journal of Biological Macromolecules*, 2021, 180: 212–221
17. Duan C, Tian C, Feng X, Tian G, Liu X, Ni Y. Ultrafast process of microwave-assisted deep eutectic solvent to improve properties of bamboo dissolving pulp. *Bioresource Technology*, 2022, 370: 128543
18. Duan C, Tian C, Tian G, Wang X, Shen M, Yang S, Ni Y. Simultaneous microwave-assisted phosphotungstic acid catalysis for rapid improvements on the accessibility and reactivity of Kraft-based dissolving pulp. *International Journal of Biological Macromolecules*, 2022, 227: 214–221
19. Tran M H, Phan D P, Lee E Y. Review on lignin modifications toward natural UV protection ingredient for lignin-based sunscreens. *Green Chemistry*, 2021, 23(13): 4633–4646
20. Kamimura N, Sakamoto S, Mitsuda N, Masai E, Kajita S. Advances in microbial lignin degradation and its applications. *Current Opinion in Biotechnology*, 2019, 56: 179–186
21. Yu M, Guo Y, Wang X, Zhu H, Li W, Zhou J. Lignin-based

- electrospinning nanofibers for reversible iodine capture and potential applications. *International Journal of Biological Macromolecules*, 2022, 208: 782–793
22. Hou C, Chen W, Fu L, Zhang S, Liang C, Wang Y. Efficient degradation of perfluorooctanoic acid by electrospun lignin-based bimetallic MOFs nanofibers composite membranes with peroxymonosulfate under solar light irradiation. *International Journal of Biological Macromolecules*, 2021, 174: 319–329
  23. Li Q, Dong M, Li R, Cui Y, Xie G, Wang X, Long Y. Enhancement of Cr(VI) removal efficiency via adsorption/photocatalysis synergy using electrospun chitosan/g-C<sub>3</sub>N<sub>4</sub>/TiO<sub>2</sub> nanofibers. *Carbohydrate Polymers*, 2021, 253: 117200
  24. Zhang X, Wang J, Dong X, Lv Y. Functionalized metal–organic frameworks for photocatalytic degradation of organic pollutants in environment. *Chemosphere*, 2020, 242: 125144
  25. Gautam S, Agrawal H, Thakur M, Akbari A, Sharda H, Kaur R, Amini M. Metal oxides and metal organic frameworks for the photocatalytic degradation: a review. *Journal of Environmental Chemical Engineering*, 2020, 8(3): 103726
  26. Wang C, Li J, Lv X, Zhang Y, Guo G. Photocatalytic organic pollutants degradation in metal–organic frameworks. *Energy & Environmental Science*, 2014, 7(9): 2831–2867
  27. Liu Y, Liu Z, Huang D, Cheng M, Zeng G, Lai C, Zhang C, Zhou C, Wang W, Jiang D, Wang H, Shao B. Metal or metal-containing nanoparticle@MOF nanocomposites as a promising type of photocatalyst. *Coordination Chemistry Reviews*, 2019, 388: 63–78
  28. Xiao J, Shang Q, Xiong Y, Zhang Q, Luo Y, Yu S, Jiang H L. Boosting photocatalytic hydrogen production of a metal–organic framework decorated with platinum nanoparticles: the platinum location matters. *Angewandte Chemie International Edition*, 2016, 55(32): 9389–9393
  29. Liu X, Dang R, Dong W, Huang X, Tang J, Gao H, Wang G. A sandwich-like heterostructure of TiO<sub>2</sub> nanosheets with MIL-100(Fe): a platform for efficient visible-light-driven photocatalysis. *Applied Catalysis B: Environmental*, 2017, 209: 506–513
  30. He W, Li Z, Lv S, Niu M, Zhou W, Li J, Lu R, Gao H, Pan C, Zhang S. Facile synthesis of Fe<sub>3</sub>O<sub>4</sub>@MIL-100(Fe) towards enhancing photo-Fenton like degradation of levofloxacin via a synergistic effect between Fe<sub>3</sub>O<sub>4</sub> and MIL-100(Fe). *Chemical Engineering Journal*, 2021, 409: 128274
  31. Lu W, Duan C, Zhang Y, Gao K, Dai L, Shen M, Wang W, Wang J, Ni Y. Cellulose-based electrospun nanofiber membrane with core-sheath structure and robust photocatalytic activity for simultaneous and efficient oil emulsions separation, dye degradation and Cr(VI) reduction. *Carbohydrate Polymers*, 2021, 258: 117676
  32. Lu W, Duan C, Liu C, Zhang Y, Meng X, Dai L, Wang W, Yu H, Ni Y. A self-cleaning and photocatalytic cellulose-fiber-supported “Ag@AgCl@MOF-cloth” membrane for complex wastewater remediation. *Carbohydrate Polymers*, 2020, 247: 116691
  33. Meng X, Duan C, Zhang Y, Lu W, Wang W, Ni Y. Corn-cob-supported Ag NPs@ ZIF-8 nanohybrids as multifunction biosorbents for wastewater remediation: robust adsorption, catalysis and antibacterial activity. *Composites Science and Technology*, 2020, 200: 108384
  34. Xie A, Cui J, Yang J, Chen Y, Dai J, Lang J, Li C, Yan Y. Photo-Fenton self-cleaning membranes with robust flux recovery for an efficient oil/water emulsion separation. *Journal of Materials Chemistry A*, 2019, 7(14): 8491–8502
  35. Zhang Q, Zhang Z, Zhao D, Wang L, Li H, Zhang F, Huo Y, Li H. Synergistic photocatalytic-photothermal contribution enhanced by recovered Ag<sup>+</sup> ions on MXene membrane for organic pollutant removal. *Applied Catalysis B: Environmental*, 2023, 320: 122009
  36. Ahmad M A T, Abdul Rahman N. Preparation and characterization of highly porous polyacrylonitrile electrospun nanofibers using lignin as soft template via selective chemical dissolution technique. *Polymers*, 2021, 13(22): 3938
  37. Zhang L, He Y, Ma L, Chen J, Fan Y, Zhang S, Shi H, Li Z, Luo P. Hierarchically stabilized PAN/β-FeOOH nanofibrous membrane for efficient water purification with excellent antifouling performance and robust solvent resistance. *ACS Applied Materials & Interfaces*, 2019, 11(37): 34487–34496
  38. Attia A A M, Abas K M, Nada A A A, Shouman M A H, Siskova A O, Mosnacek J. Fabrication, modification, and characterization of lignin-based electrospun fibers derived from distinctive biomass sources. *Polymers*, 2021, 13(14): 2277
  39. Du X, Yi X, Wang P, Deng J, Wang C. Enhanced photocatalytic Cr(VI) reduction and diclofenac sodium degradation under simulated sunlight irradiation over MIL-100(Fe)/g-C<sub>3</sub>N<sub>4</sub> heterojunctions. *Chinese Journal of Catalysis*, 2019, 40(1): 70–79
  40. Duan C, Meng J, Wang X, Meng X, Sun X, Xu Y, Zhao W, Ni Y. Synthesis of novel cellulose-based antibacterial composites of Ag nanoparticles@metal–organic frameworks@carboxymethylated fibers. *Carbohydrate Polymers*, 2018, 193: 82–88
  41. Jia D, Xie J, Dirican M, Fang D, Yan C, Liu Y, Li C, Cui M, Liu H, Chen G, Zhang X, Tao J. Highly smooth, robust, degradable and cost-effective modified lignin-nanocellulose green composite substrates for flexible and green electronics. *Composites Part B: Engineering*, 2022, 236: 109803
  42. Gao K, Shen M, Duan C, Xiong C, Dai L, Zhao W, Lu W, Ding S, Ni Y. Co-N-doped directional multichannel PAN/CA-based electrospun carbon nanofibers as high-efficiency bifunctional oxygen electrocatalysts for Zn-air batteries. *ACS Sustainable Chemistry & Engineering*, 2021, 9(50): 17068–17077
  43. Wang R, Xu H, Liu X, Fang D, Wei S, Yu A N. *In-situ* growth of iron oxides with MIL-100(Fe) enhances its adsorption for selenite. *Surfaces and Interfaces*, 2022, 34: 102325
  44. Zhang X, Qi Y, Yang J, Dong S, Liu J, Li J, Shi K. Insight into stabilization behaviors of lignin/PAN-derived electrospun precursor fibers. *Polymer Degradation & Stability*, 2021, 191: 109680
  45. Lei M, Wang N, Zhu L, Tang H. Peculiar and rapid photocatalytic degradation of tetrabromodiphenyl ethers over Ag/TiO<sub>2</sub> induced by interaction between silver nanoparticles and bromine atoms in the target. *Chemosphere*, 2016, 150: 536–544
  46. Wali L A, Alwan A M, Dheyab A B, Hashim D A. Excellent fabrication of Pd–Ag NPs/PSi photocatalyst based on bimetallic nanoparticles for improving methylene blue photocatalytic degradation. *Optik*, 2019, 179: 708–717
  47. Wang R, Zhong Y, He R, Zou Y, Yang J, Fu M, Zhang R, Zhou

- Y. Ultrahigh emulsion separation flux and antifouling performance of MIL-100(Fe)@Graphene oxide membrane enabled by its superhydrophilicity and self-cleaning ability. *Advanced Sustainable Systems*, 2022, 6(6): 2100497
48. Li Q, Deng W, Li C, Sun Q, Huang F, Zhao Y, Li S. High-flux oil/water separation with interfacial capillary effect in switchable superwetting Cu(OH)<sub>2</sub>@ZIF-8 nanowire membranes. *ACS Applied Materials & Interfaces*, 2018, 10(46): 40265–40273
49. Su S, Xing Z, Zhang S, Du M, Wang Y, Li Z, Chen P, Zhu Q, Zhou W. Ultrathin mesoporous g-C<sub>3</sub>N<sub>4</sub>/NH<sub>2</sub>-MIL-101(Fe) octahedron heterojunctions as efficient photo-Fenton-like system for enhanced photo-thermal effect and promoted visible-light-driven photocatalytic performance. *Applied Surface Science*, 2021, 537(2021): 147890
50. Duan S, Li J, Liu X, Wang Y, Zeng S, Shao D, Hayat T. HF-free synthesis of nanoscale metal–organic framework NMIL-100(Fe) as an efficient dye adsorbent. *ACS Sustainable Chemistry & Engineering*, 2016, 4(6): 3368–3378
51. Molavi H, Hakimian A, Shojaei A, Raeiszadeh M. Selective dye adsorption by highly water stable metal–organic framework: long term stability analysis in aqueous media. *Applied Surface Science*, 2018, 445: 424–436
52. Yang L, Xiang Y, Jia F, Xia L, Gao C, Wu X, Peng L, Liu J, Song S. Photo-thermal synergy for boosting photo-Fenton activity with rGO-ZnFe<sub>2</sub>O<sub>4</sub>: novel photo-activation process and mechanism toward environment remediation. *Applied Catalysis B: Environmental*, 2021, 292: 120198